Postprint **Permeability evolution in open fractures during precipitation and dissolution – A phase-field study** by M. Späth, B. Nestler.
Accepted for publication in Advances in Water Resources on Oct 16, 2023.
Original publication: https://doi.org/10.1016/j.advwatres.2023.104563

Permeability evolution in open fractures during precipitation and dissolution – A phase-field study

Michael Späth[a], Britta Nestler[a,b]

[a] *Institute of Nanotechnology (INT-MSS), Karlsruhe Institute of Technology (KIT), Hermann-von-Helmholtz-Platz 1 ,76344 Eggenstein-Leopoldshafen,Germany*
[b] *Institute for Applied Materials (IAM-MMS), Karlsruhe Institute of Technology (KIT), Straße am Forum 7, 76131 Karlsruhe, Germany*

Abstract

In dilated fractures in the Earth's crust fluid flow in combination with precipitation or dissolution processes can occur, which in turn influences the mechanical and transport properties of the rock system. We use a phase-field modeling framework to investigate these processes of epitaxial crystal growth and dissolution on the fracture walls of crystalline rock systems on microscale. Fluid flow simulations are performed and analyzed during intermediate crystallization and dissolution stages and the obtained hydraulic properties of the partly open fractures are compared to existing literature. The systematic simulation studies show how the rock properties are affected by factors as mineral type with different crystal morphologies, fracture type (inter- vs. transgranular), aperture of the open fracture, and presence of accessory minerals. The results indicate that within the considered parameter space the flow paths remain open until late stages of fracture sealing. Moreover, the long-term permeability and porosity evolution is strongly affected by fracture surface heterogeneities and initial fracture apertures. The simulations enable insights into the evolution of microstructural and fluid flow characteristics and can lay the basis for applications in fractured porous media as groundwater protection, geothermal and hydrocarbon reservoir prediction, water recovery, or storing H_2 or CO_2 in the subsurface.

Keywords: fluid flow, permeability evolution, fractured rock, crystallization, dissolution

1. Introduction

The flow of fluids in open fractures is a fundamental process in rock systems in the upper and middle crust. Fractures can form and widen during deformation and induce fluid pathways. In these dilated fractures crystal growth or dissolution processes can occur depending on the chemical conditions of the

Corresponding author: Michael Späth (michael.spaeth@kit.edu)

aqueous fluid (e.g., saturation state), which in turn affects the rock properties of the subsurface system (e.g., strength, permeability). A deeper understanding of the processes of fluid flow and how it is affected by crystallization or dissolution is of great importance to different fields of basic or applied geosciences, i.e. injection and production of fluids from the subsurface, water production, pollutant transport, wastewater storage, geothermal energy production, or storage of hydrogen, heat, or carbon dioxide [1–9].

In the last decades an extensive amount of experimental and numerical studies were presented discussing effects of various factors, which control the fluid flow behavior and the resulting permeability in open fractures and fracture networks at different length scales (centimeter to reservoir scale). For an overview of fluid flow in fractured media and the advances and open issues we refer to review articles of Berkowitz [10], Liu et al. [11] and Viswanathan et al. [12], whereas an overview of coupled thermal, hydraulic, mechanical, and chemical (THMC) processes and their effects on the corresponding subsurface environments is given for example in Tsang [13], Rutqvist and Stephansson [14] and Laubach et al. [15].

The fluid flow in the open fractures on a local level can be influenced by different factors. Here, we distinguish between chemically active and inactive fractures. In chemically inactive fractures the fluid is in (near) equilibrium and the fracture surface does not change over time, whereas in chemically active fractures an over- or undersaturated fluid causes precipitation or dissolution (Fig. 1). In chemically inactive fractures the flow path of the fluid can be affected by the fracture roughness (e.g., Hurst coefficient) or in case of complex stress states also by a sheared widening of the two fracture surfaces, which can cause anisotropic flow paths or the formation of fluid channels. In chemically active fractures the evolving crystal structure and therefore the corresponding fluid pathways can depend for example on the evolving crystal structures or on the presence of accessory minerals. Additionally, the fluid flow in chemically active and inactive fractures can be affected by mechanical activity (e.g. renewed or continuous opening due to thermal, chemical and/or mechanical stresses). For example, when a fracture is chemically and mechanically active, multi-crack-sealing can occur, which might result in radiator-fin crystal structures or isolated crystal bridges [16–18], whereas in chemically inactive fractures a mechanical activity can result in a continuous widening and/or shearing.
The analysis of natural partly filled fractures helps to improve the understanding of how fractures and cement affecting overall permeability and fluid flow in complex fracture systems. For example, different works shed light on how quartz deposits reduce the open fracture connectivity in tapering fracture tips (due to quartz accumulation) [19], or how fluid flow is affected in variably cemented fracture networks where part of the flow is through porous host rock [20].
With laboratory experiments a better understanding of fluid flow processes in chemically active and inactive fractures can be obtained. They enable the mea-

surement of hydraulic conductivities of natural fractured rock [21] or a validation to analytical flow models [22, 23]. Moreover, laboratory hydrothermal flow-through experiments allow investigations on chemically active fractures where characteristic properties change over time. These experiments can assist the understanding of processes occurring in fractured rock during crystallization or dissolution and were performed for various minerals which are present in the Earth's crust [24–32].

Fracture apertures can be used in analytical or empirical equations to esti-

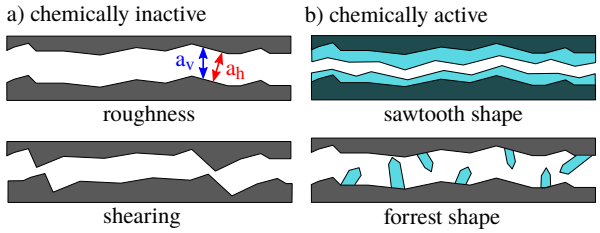

Figure 1: Different characteristics of open fractures affecting fluid flow during crystal growth and dissolution. a) In chemically inactive fractures the roughness (top) and opening trajectory like shearing (bottom) and b) in chemically actives fractures precipitation or dissolution can affect the fluid properties. In a) the difference between the vertical a_v and hydraulic aperture a_h is indicated.

mate the resulting permeability [22] in single fractures, whereas on larger length scales (e.g., fracture networks) the length distribution and host porosity with connectivity plays an important role on the resulting permeability (e.g., [33]). In Fig. 1a the difference between the vertical/mechanical aperture a_v and the hydraulic/effective aperture a_h is visualized. The vertical aperture is the distance between the two fracture surfaces, whereas the hydraulic aperture corresponds to the aperture in a (local) parallel plate equivalent case. It is mostly smaller than vertical aperture and can be estimated for example with empirical laws where characteristic features of the crack (e.g., roughness, fracture geometry) are related with the vertical aperture. There are numerous works available how the hydraulic aperture can be determined and we refer to Table 1 in Kling et al. [34] for an overview of different estimations of a_h and their space of validity.

In recent years, computational modeling of fluid flow in chemically active and inactive open fractures has emerged as an alternative to laboratory experiments since it helps to predict and quantify physical processes not easily obtainable in experiments. An overview of different approaches of fluid flow modeling in fractured rock is given in Berre et al. [35]. For example, fluid flow was investigated in rough inert fractures on centimeter scale for low [36] and higher flow velocities [37] or during the formation of fracture networks (e.g., Paluszny et al. [38]). In chemically active fractures, numerical approaches can help to understand the crystallization process and the development of fluid flow during the precipitation. Early on, sharp interface front-tracking models were used to pre-

dict the evolving microstructures in open fractures [39–42]. Moreover, cellular automaton programs were applied for crystal growth processes in subsurface environments [17, 43] and provide valuable insight into the crystallization process within their modeled 2D structures.
Additionally, different numerical techniques were applied to investigate dissolution processes on grain scale in a diverse range of minerals [44–46]. For example, with approaches like the Monte Carlo Method [44], Level-Set Method [47], Dynamic Mesh techniques [48], Discrete Element Method, or Bonded-Particle Method [49] the influence of the chemical and mechanical properties of microstructures during mineral dissolution were analyzed.

Besides the previous mentioned approaches, the phase-field method also enables the modeling of phase transition processes. Within this simulation technique a mathematical model is used to describe interfaces (e.g., grain boundaries, fluid-solid surface) in a diffuse manner and therefore avoids the necessity of using remeshing or complex interface tracking algorithms. In material science the phase-field method is widely used and applied to multi-physics applications since it allows the incorporation of additional physical fields into the phase evolution process (e.g. temperature, concentration, or mechanics [50–53]).
Besides material science, phase-field modeling has also been used in geoscience applications on microscale such as precipitation or dissolution of minerals in hydrothermal environments. The evolution of crystal structures during precipitation was investigated for example in reservoirs [54–56] and open fractures [18, 57–63]. The effects on how crystals grow and interact with fluid flow during precipitation in open cracks is explored in Kling et al. [34], Spruženiece et al. [60], Späth et al. [64]. In Kling et al. [34] the permeability evolution in chemically active fractures is evaluated and a relationship for the prediction of the hydraulic aperture is given. The obtained data is compared to literature data, whereas the presented equation shows a good agreement over a large range of fracture roughnesses.
Moreover, crystal dissolution of different minerals in undersaturated fluids has been modeled for example in fractured rocks or reservoirs rocks [47, 65–68].

Even though previous works focused on the microstructural evolution in open fractures or investigated fluid flow in static fractures, a detailed analysis of chemically active fractures during precipitation and dissolution with different minerals and crystal habits has not been presented so far. Here, we expand on the previous modeling works of crystal evolution processes from Ankit et al. [57], Wendler et al. [58], Prajapati et al. [59] and extend the works of Kling et al. [34], Spruženiece et al. [60] to give further insight into the permeability evolution in a single chemically active fracture during precipitation and dissolution on microscale.

2. Methods

In this work we use the phase-field method for modeling the crystal evolution during precipitation and dissolution in single fractures on microscale. The presented model is based on the work of Nestler et al. [69] and was used in previous works Spruženiece et al. [60, 61]. In this section the main model equations are briefly reiterated and the simulation procedure with the used boundary conditions is presented. For a detailed description of the model formulations for crystal growth we refer to Prajapati et al. [56], Ankit et al. [57], Wendler et al. [58], Spruženiece et al. [60] and for crystal dissolution to Prajapati et al. [67].

2.1. Multiphase-field model for crystal growth and dissolution

We consider a physical domain V, in which N scalar-valued order parameters $\phi_\alpha(\boldsymbol{x}, t)$ are present. For the sake of a compact notation they are collected in the phase-field tuple $\boldsymbol{\phi}(\boldsymbol{x}, t) = [\phi_1(\boldsymbol{x}, t), \ldots, \phi_N(\boldsymbol{x}, t)]$, whereas bold symbols denote vector quantities or tuples and non-bold symbols refer to scalar-valued quantities. The phase-field parameter $\phi_\alpha(\boldsymbol{x}, t) \in [0, 1]$ describes the presence of a particular crystal or liquid phase at position $\mathbf{x}$ and time t. Within the phase-field approach the interface between phases is characterized by a diffuse interface region, where the order parameter ϕ_α continuously increases from 0 (not present) to 1 (bulk phase) (Fig. 2a). Also, the validity of the summation constraint $\sum_{\alpha=1}^{N} \phi_\alpha = 1$ is guaranteed at each computational grid point at all times. The temporal evolution of the order parameters characterizes the presence of the phases and therefore obviates the necessity of additional interface tracking algorithms.

The evolution equation is based on a local minimization of the free energy

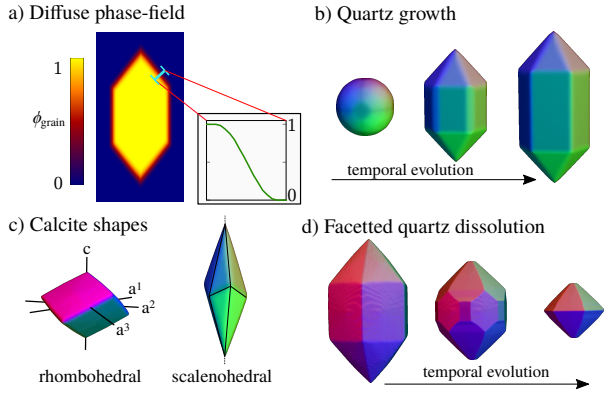

Figure 2: Crystal growth and dissolution within the phase-field approach. a) 2D-cut of quartz crystal with diffuse interface region, where the order parameter increases continuously from 0 to 1. b) Faceted crystal growth of a quartz grain starting from a sphere (e.g., Prajapati et al. [56], Wendler et al. [58]). c) Crystal shapes of rhombohedral and scalenohedral calcite (e.g., Spruženiece et al. [60, 61]). d) Temporal evolution of faceted crystal dissolution of a quartz crystal (e.g., Prajapati et al. [67])).

functional and is given by [70]

$$\frac{\partial \phi_\alpha}{\partial t} = -\frac{1}{N\epsilon} \sum_{\substack{\beta=1 \\ \beta \neq \alpha}}^{N} \left[M_{\alpha\beta}(\hat{\boldsymbol{n}}) \left(\frac{\delta \mathcal{F}_{\mathrm{intf}}}{\delta \phi_\alpha} - \frac{\delta \mathcal{F}_{\mathrm{intf}}}{\delta \phi_\beta} - \frac{8\sqrt{\phi_\alpha \phi_\beta}}{\pi} \left(\frac{\delta \mathcal{F}_{\mathrm{bulk}}}{\delta \phi_\beta} - \frac{\delta \mathcal{F}_{\mathrm{bulk}}}{\delta \phi_\alpha} \right) \right) \right], \tag{1}$$

with the mobility $M_{\alpha\beta}$ of the α-β interface. The free energy functional $\mathcal{F}(\boldsymbol{\phi}, \boldsymbol{\nabla \phi})$ is denoted with

$$\mathcal{F}(\boldsymbol{\phi}, \boldsymbol{\nabla \phi}) = \int_\Omega \left[f_{\mathrm{bulk}}(\boldsymbol{\phi}) + \epsilon a(\boldsymbol{\phi}, \nabla \boldsymbol{\phi}) + \frac{\omega(\boldsymbol{\phi})}{\epsilon} \right] \mathrm{d}V = \mathcal{F}_{\mathrm{bulk}} + \mathcal{F}_{\mathrm{intf}}, \tag{2}$$

and comprises the terms of the bulk free energy density $f_{\mathrm{bulk}}(\phi)$, the potential energy density $w(\phi)/\epsilon$, and the gradient energy density $\epsilon a(\phi, \nabla \phi)$. The first term corresponds to the chemical driving force, whereas the second and third terms represent interfacial energy density contributions. Furthermore, ϵ denotes a small length scale parameter related to the interface thickness. We utilize a multi-obstacle potential energy density [69] and model the crystal growth and dissolution with an anisotropic gradient energy density and kinetic mobility. The gradient energy density

$$\epsilon a(\boldsymbol{\phi}, \nabla \boldsymbol{\phi}) = \epsilon \sum_{\alpha=1}^{N} \sum_{\beta>\alpha}^{N} \gamma_{\alpha\beta} a_{\alpha\beta}^2(\boldsymbol{\phi}, \nabla \boldsymbol{\phi}) |\mathbf{q}_{\alpha\beta}|^2, \tag{3}$$

comprises the generalized gradient $\mathbf{q}_{\alpha\beta} = \phi_\alpha \boldsymbol{\nabla} \phi_\beta - \phi_\beta \boldsymbol{\nabla} \phi_\alpha$, in which $\gamma_{\alpha\beta}$ is the surface energy density of the α-β interface. The normalized interface normal vector is given by $\hat{\boldsymbol{n}} = \mathbf{q}_{\alpha\beta}/|\mathbf{q}_{\alpha\beta}|$. With the factor

$$a_{\alpha\beta}(\boldsymbol{\phi}, \nabla \boldsymbol{\phi}) = \max_{1 \leq k \leq n_{\alpha\beta}} \left\{ \hat{\boldsymbol{n}} \cdot \eta_{k,\alpha\beta} \right\}, \tag{4}$$

a crystalline anisotropy can be prescribed. The chosen crystal habit is described with its Wulff shape with a total number of $n_{\alpha\beta}$ corners, where $\eta_{k,\alpha\beta}$ is the vector to one particular corner.
Furthermore, the mobility of the α-β interface is given by

$$M_{\alpha\beta}(\hat{\boldsymbol{n}}) = M_{\alpha\beta}^0 a_{\alpha\beta}^{\mathrm{kin}}(\hat{\boldsymbol{n}}), \tag{5}$$

where $M_{\alpha\beta}^0$ denotes the kinetic coefficient and $a_{\alpha\beta}^{\mathrm{kin}}(\hat{\boldsymbol{n}})$ the anisotropy term. We use the formulation of Wendler et al. [58] for the anisotropy term, which enables the modeling of faster crystal growth of rough faces and a decreased growth rate once the faces reach euhedral shape and additionally allows the modeling of faceted crystal dissolution. Note: This two-rate option of the crystal growth velocities is reversible since it depends on the current state of a crystal surface and can, for example, switch back from slow euhedral to fast anhedral growth (e.g. if a spanning crystal is rebroken [17, 18]).

The multiphase-field model equations are implemented in the inhouse solver package PACE3D. For implementation details and a description of optimization algorithms, we refer to Hötzer et al. [71]. In the crystal growth and dissolution simulations a zero-gradient boundary condition at the lower and upper boundary (y-direction) is applied, whereas the other boundaries are set to be periodic (Fig. 3). In the present work a constant chemical driving force approach is used for the crystal growth and dissolution. This assumes a continuous inflow of a constant over- or undersaturated fluid in the open fracture and slow attachment or detachment kinetics compared to the fluid flow.

2.2. Fluid flow in partly open fractures

For the computation of the fluid flow the sharp interface data is extracted at intermediate growth or dissolution stages from the diffuse phase-field simulations. This microstructure is used as an input for the fluid flow simulations in the inhouse software PACE3D. We compute the incompressible stationary Stokes equations with no body forces (e.g. gravity), which assumes low flow velocities in the simulation domain (Reynolds number $\mathrm{Re} \ll 1$). The balance equations for mass and linear momentum are denoted as

$$\mu \Delta \mathbf{u} - \nabla p = 0, \tag{6}$$

$$\nabla \cdot \mathbf{u} = 0, \tag{7}$$

in which $\mathbf{u}$ is the fluid velocity, μ is the dynamic viscosity, and ∇p is the pressure gradient.

We apply a pressure gradient along x-direction and set the boundaries in z-direction periodic (Fig. 3). At the interface between the crystal growth front and the fluid a no-slip condition is prescribed: $\mathbf{u}_{\text{gr.-liq.}} = \mathbf{0}$. Similarly as in Prajapati et al. [56] we use the fluid properties of water at 20 °C ($\mu = 0.001\,002\,6\,\mathrm{kg\,m^{-1}\,s^{-1}}$ [72], $\rho = 998.203\,\mathrm{kg\,m^{-3}}$ [73]) and apply a pressure gradient of $0.58 \times 10^{-3}\,\mathrm{Pa\,m^{-1}}$ to ensure small Reynolds numbers and the validity of the Stokes equations.

For the computation of the permeability in the fluid flow we use Darcy's law

$$Q = \frac{Ak}{\mu} \nabla p \tag{8}$$

with the flow rate Q, the cross-sectional area of the fracture A, and the permeability k. The cubic law relates the flow rate in a domain with width W to the aperture a for two parallel plates and is given by

$$Q = \frac{a^3 W}{12\mu} \nabla p. \tag{9}$$

Moreover, the permeability can be expressed as

$$k = \frac{a^2}{12}, \tag{10}$$

when the relationship $A = aW$ is used. Alternatively, the fracture transmissivity (per unit length) $T = a^3/12$ [74] shows a direct connection to the cubic law. For estimating the hydraulic aperture a_h we utilize the equation introduced in Kling et al. [34]

$$a_h = a_v \left(1 + \alpha \frac{\sigma}{a_v}\right)^{-\frac{3}{2}} \tag{11}$$

where a_v is the vertical aperture, σ is the standard deviation of a_v and α is a geometry factor depending on the crystal shape. In Kling et al. [34] this factor was determined for needle shaped quartz to $\alpha = 2.5$ and for compact quartz to $\alpha = 1.0$.
Additionally, in order to quantify the deflection of the fluid flow during the precipitation and dissolution we evaluate the deflection of the flow path $\tau_h = |\mathbf{u}|/u_x$ [75] with the fluid velocity in flow direction u_x and the absolute value of the fluid velocity $|\mathbf{u}|$. For undisturbed fluid flow fields the deflection of the flow path equals one, whereas $\tau_h > 1$ implies a distorted flow path.

2.3. Crystal shapes and parameters

Quartz growth. Quartz can exhibit a broad variety of crystal habits in natural environments (e.g., Goldschmidt [76]). For the sake of simplicity we utilize in this work a commonly observed crystal shape in nature, namely prismatic bipyramidal crystal shape. This shape has been also used in previous phase-field studies [56, 58] and therefore we directly apply the vector set for the capillary and kinetic anisotropy and the used physical conditions with the corresponding non-dimensionalization from Wendler et al. [58]. In this work we focus on crystal growth in a host rock with randomly oriented grains with a gaussian distribution (see Section 2.4) which is fractured only once (mechanically inactive). The influence of preferred grain orientations in the host rock or nucleation substrate effects like grain surface coatings or lattice defects (e.g. dislocations) are not explicitly considered in the present work. Note that effects of the different (randomly distributed) crystal orientations during crystal growth and effects of different crystal sizes in the host rock are visible in the crystal growth simulations. For example, larger grains in contact with the liquid grow faster (take longer to reach euhedral shape) and have the potential to overgrow smaller crystals. Additionally, mechanical effects could be incorporated in future works [18, 77]. The corresponding temporal evolution of the growth of a single quartz crystal starting from a sphere is depicted in Fig. 2b.

Calcite growth. In limestones minerals as calcite, dolomite, and aragonite are present and can show various crystal habits depending on the physical and chemical conditions (e.g. temperature, supersaturation, impurities) of the fluid-rock system. Similarly as in the previous works of Spruženiece et al. [60, 61], Späth et al. [62], we focus on calcite and choose a rhombohedral and scalenohedral crystal habit (Fig. 2c), since they are commonly observed in natural systems [78]. The vectors for the kinematic and capillary anisotropy of both crystal habits

are given in Späth et al. [62]. In contrast to the precipitation of quartz we did not perform an explicit non-dimensionalization of the phase-field parameters with fluid properties (e.g., p, c, T) and chose the used parameters to obtain a numerically stable simulation while also reducing computational costs. Note: When additional physical properties are available a mapping of the phase-field parameters is possible like in the case of quartz growth.

Faceted dissolution of quartz. The dissolution of quartz is a complex process and the resulting shape evolution can be dependent on various parameters like chemical composition of the fluid (pH, dissolved ions), dominant mechanisms (surface desintegration, bulk diffusion) and their dependencies on physical conditions. Therefore, the occurrence of distinct facets (which appear and disappear at unequal rates) can be affected by temperature [79], saturation state [80], molal concentration and presence of cations/salt effect [81], pH [82], particle size [83], and crystal defects [84]. In this work the modeling approach of Prajapati et al. [67] is used with the therein given parameters since the modeling results show a quantitative agreement with literature data. For a detailed description of the derivation of the parameters and crystal shapes we refer to Prajapati et al. [67]. The resulting temporal evolution of a single quartz grain during dissolution is depicted in Fig. 2d.

2.4. Simulation procedure of the phase-field models

The numerical host rock which is used for the crystal growth and dissolution simulations is generated in a multi-step process. First, a polycrystalline rock structure is generated with a Voronoi tessellation where 8,000 or 16,000 grains are randomly distributed in the simulation domain for the precipitation and dissolution case respectively (Fig. 3a). Then, a spectral synthesis method [36, 85] is utilized to generate a fractal fracture surface (Fig. 3b). A roughness/Hurst exponent of $H = 0.8$ is chosen for the generated structures, since it is a typical value for natural crystalline rocks as granite [86, 87].

In the second step, the host rock and the fractal surface are combined (Fig. 3c)

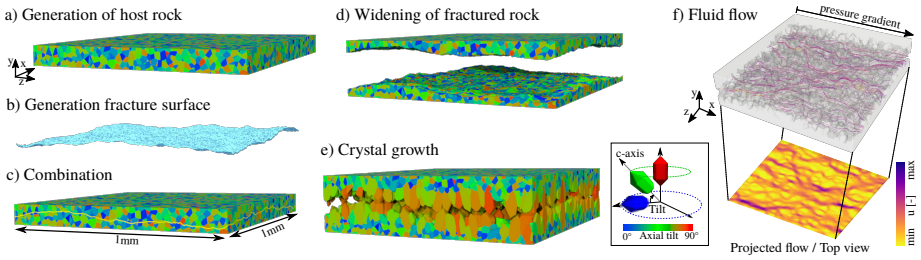

Figure 3: Schematic workflow. a) A host rock and b) fractal surface are generated and c) combined. After the fractured rock is widened (in d)) precipitation or dissolution are initiated (in e)). f) In intermediate growth stages fluid flow simulations are performed. The color of a phase indicates the orientation of a grain (color bar between e) and f)).

and the fracture is widened in y-direction (pure normal opening) in a single

step (Fig. 3d). This combination of fracture surface and host rock results in mostly pure transgranular fractured grains, where crystal fragments are present in the upper and lower fracture wall. The aperture is chosen between 2-10 D_m, where D_m is the average host rock grain diameter and enables a direct comparison to different types of natural partly or fully sealed fractures, where the size of the host rock grains can differ. An equidistant orthogonal grid with 1000×1000×139-537 cells is used, whereas one cells corresponds to 1 µm and the average host grain diameter D_m is 27 µm. For the dissolution case, the open fracture is widened with an aperture of 0.8 D_m and then shifted in x- and z-direction until the fracture surfaces are partly in contact again. The simulation domain consists of 1000×1000×366 cells ($\Delta x = 1$ µm). In the next step, the crystal growth or dissolution is initiated (Fig. 3e) and the phase-field simulations stop, once the (partly) open fracture is completely sealed or dissolved. The grains in the initial host rock are normally distributed with a standard deviation of 0.0743 D_m.
In intermediate growth stages fluid flow simulations are performed to compute the permeability or transmissivity evolution. For a compact visualization we show in the forthcoming sections the projected fluid flow/top view (Fig. 3f) which gives the average fluid flow velocity along the y-direction instead of a streamline visualization.

3. Results

3.1. Precipitation in quartz microstructure

In this section the effects of crystallization in a single open fracture on the fluid flow evolution is investigated in a quartz microstructure. The numerical host rock is monomineralic (no accessory minerals) and no pores are present, which corresponds for example to metamorphic quartzite. In the first study we focus on crystal growth in an open crack with an aperture of 4 D_m. The temporal evolution of the crystal structure, the fluid pathways, and the remaining aperture in the open crack are depicted in Fig. 4a-c respectively during four representative time-steps ①-④. Note that the color bar for the fluid flow is different in each time-step to improve the visibility of the characteristic features of the fluid flow development (from slight deflection of fluid paths to formation of channels). The initial aperture (①) shows a uniform distribution due to the normal widening of the fracture and the fluid flow shows only small deviations in the fluid velocity due to the rough fracture surface. After approximately 25% of sealing a deviation in the aperture distribution between mean and minimal aperture is visible (Fig. 4d) since the quartz crystals with a vertical c-axis grow faster into the open fracture (②) and their tips interact with the fluid stream, whereas regions with unfavorably oriented crystals leave more space for the fluid flow. When 40% of the fracture is sealed the first crystals bridge the open fracture (③) and the shape of the fluid pathways changes drastically with implications for the fluid connectivity. We observe the appearance of fluid channels which are caused by crystal pillars deflecting the fluid. This behavior

is also visible in the corresponding plot in Fig. 4e. The deflection of the fluid paths continuously increases with the increase of crystal bridges in the partly open crack. When approximately 80% of the fracture is sealed (④) the majority of the open crack contains crystal pillars which results in a further decrease of the fluid velocity due to the applied constant pressure drop. Additionally, blood vessel shaped fluid paths evolve here due to the presence of fluid channels and sealed regions (where no flow occurs). In the nearly cemented fracture both stretched and blocky crystals are present, which results from the pure transgranular fracturing in the host rock. When the same crystal fragments from opposite walls touch, stretched crystals form, whereas blocky grains form where crystals from different fragments meet in the middle of the fracture.

In addition to the previous case with an aperture of $4\,D_m$ we also investi-

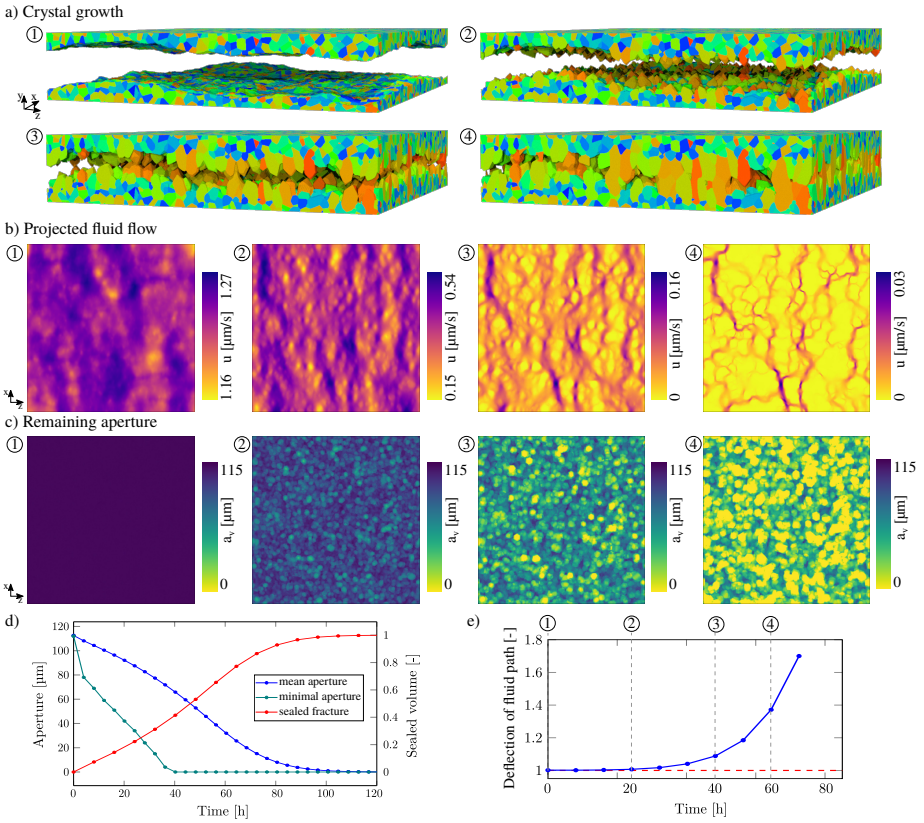

Figure 4: Precipitation of quartz in an open fracture with an aperture of $4\,D_m$. a) Temporal evolution of the crystal structure, b) fluid flow in a projected view, and c) remaining vertical aperture in open fracture are given for four time-steps 1-4. d) Evolution of the mean and minimal aperture and the sealing state (amount of fluid porosity) in the fracture. e) Deflection of the fluid flow paths during the precipitation. The four time-steps 1-4 are highlighted.

gate the evolution of fluid flow with fracture apertures of 2-10 D_m (Fig. 5). The transmissivity evolution over time is evaluated for each aperture and compared to the cubic law (Eq. (10)). For the computation of the vertical aperture we arithmetically averaged the local apertures [34, 88] to enable a direct comparability to Kling et al. [34]. The transmissivity decreases continuously over time during crystal growth (Fig. 5a). For the aperture of 2 D_m the measured transmissivity is comparatively close to the cubic law for early time-steps and only shows a deviation in late sealing states when most of the fracture is closed. This can be attributed to the relatively small aperture which closes fast and few crystal peaks interact with the fluid (surface stays closer to parallel plates). This behavior of relatively homogeneous apertures over time is also visible in the plot of vertical apertures with their standard deviations (Fig. 5b). We also plot the relative surface roughness $\xi = \sigma/a_v$ in Fig. 5c which increases over time and is used for the computation of the hydraulic aperture in Eq. (11). As expected, for increasing initial apertures a deviation between the simulated transmissivity and the cubic law arises since fast growing crystals cause a rougher and inhomogeneous surface and deflect the fluid paths more.

Furthermore, we analyze the occurrence of isolated pores in the open crack

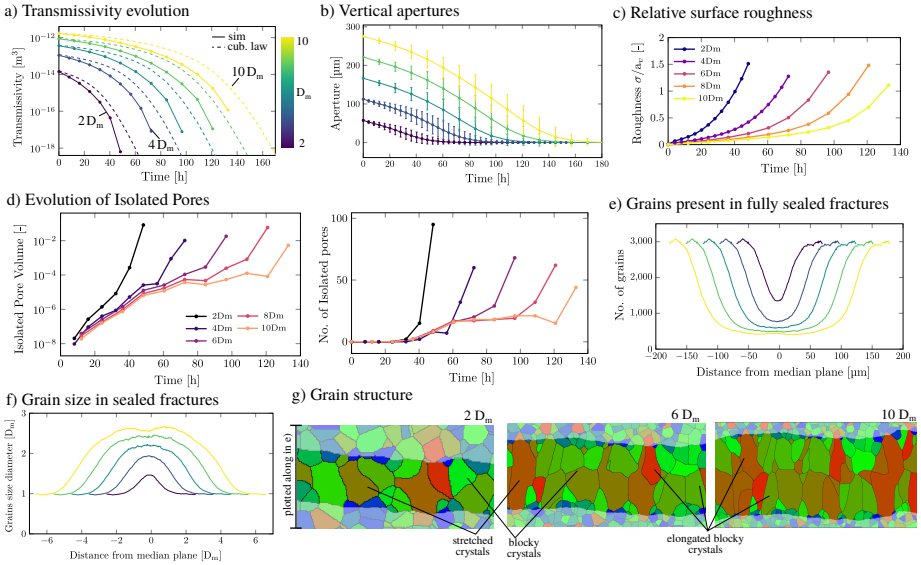

Figure 5: a) Transmissivity evolution of the initial fracture apertures of $2, 4, 6, 8$, and $10\,D_m$. The measured transmissivity from the phase-field simulations and the transmissivity calculated with the cubic law is plotted. b) Evolution of the vertical aperture with the standard deviations for the five aperture. The color bar is the same as in a). c) Plot of the relative fracture roughness in the simulations. d) Evolution of the number of isolated pores (right) and the isolated pore volume (left). e) Number of grains and f) corresponding crystal size in fully sealed fractures along the vertical (y-)direction (color bar in a). g) Resulting microstructure in fully sealed fractures exemplary displayed for 2, 6, and $10\,D_m$ aperture with characteristic crystal shapes. The line on the left indicates the direction of the plot in e).

during sealing (Fig. 5d). Isolated pores can occur when either multiple crystals from the opposite fracture walls touch and form a pore which is not connected to the fluid flow or due to growth competition between favorably and unfavorably oriented crystals on one fracture wall. The first case occurs in later sealing stages, whereas the second case more likely appears during early time-steps when growth competition is dominant. The amount of isolated pores and its volume is relatively small in the beginning and starts to rapidly increase once the crystal bridges. For this analysis, the volume of isolated pores is measured and then normalize to the total volume of the open fracture. A pore is considered isolated, when it has no connectivity to the fluid flowing through the (partially) open fracture. To quantify this case, we used a flood fill algorithm to determine if a *liquid region* is surrounded by grains/rock only (isolated pore) or has connectivity to the fluid flow region (where the fluid velocity is non-zero). In the fully sealed fracture the number of present grains decreases from the host rock into the center of the vein due to growth competition (Fig. 5e), whereas the size of the crystals in the sealed fracture increases accordingly (Fig. 5f). For this, the fully sealed vein is sliced equidistantly (in y-direction with a slice thickness of 1 µm) and the occurring crystals/present phases in each slice are counted. We observe the formation of more blocky and stretched crystals in the $2\,D_m$ vein and more elongated blocky grains for larger aperture due to an increased termination of misoriented crystals at the fracture rim (Fig. 5g). This behavior resembles microstructures in partly to fully mineral filled opening-mode fractures and is consistent to the 2D simulations presented in Späth et al. [62].

3.2. Precipitation in limestone

Here, we focus on the precipitation of calcite in open fractures and its influence on fluid flow. We use the same initial host rock as in the previous section, which corresponds to monomineralic limestone with no host rock porosity. In the first case the behavior of rhombohedral and scalenohedral calcite in an open crack with an aperture of $8\,D_m$ is tested. In Fig. 6a the lower fracture surface with rhombohedral and scalenohedral calcite is shown in an intermediate sealing stage (same amount of precipitated calcite) where the crystals from the opposite wall have not touched yet. The fracture with scalenohedral calcite shows a highly serrated and inhomogeneous growth front, whereas the rhombohedral calcite shows a relatively homogeneous growth front. This difference results from the elongated c-axis of scalenohedral calcite compared to the rhombohedral shape. Due to this deviation of the growth front the resulting fluid pathways also show a different trend for the two crystal shapes (Fig. 6b,c). The serrated growth front of the scalenohedral shape causes a stronger deflection of the fluid stream in earlier time-steps. Since the crystals also bridge earlier in the scalenohedral case (compared to same amount of precipitated calcite) fluid channels and blood vessel stream lines also occurs earlier. In the rhombohedral case the growth front remains more homogeneous until later stages of sealing and therefore the flow paths remain more homogeneous compared to the scalenohedral case. Only when the sealing is advanced and the crack is nearly

closed, the flow becomes heterogeneous as in the scalenohedral case. As a result the deflection of the flow path of the scalenohedral calcite is higher compared to the rhombohedral case until very late stages of sealing (Fig. 6d).

The corresponding permeability-porosity relationship and the comparison to

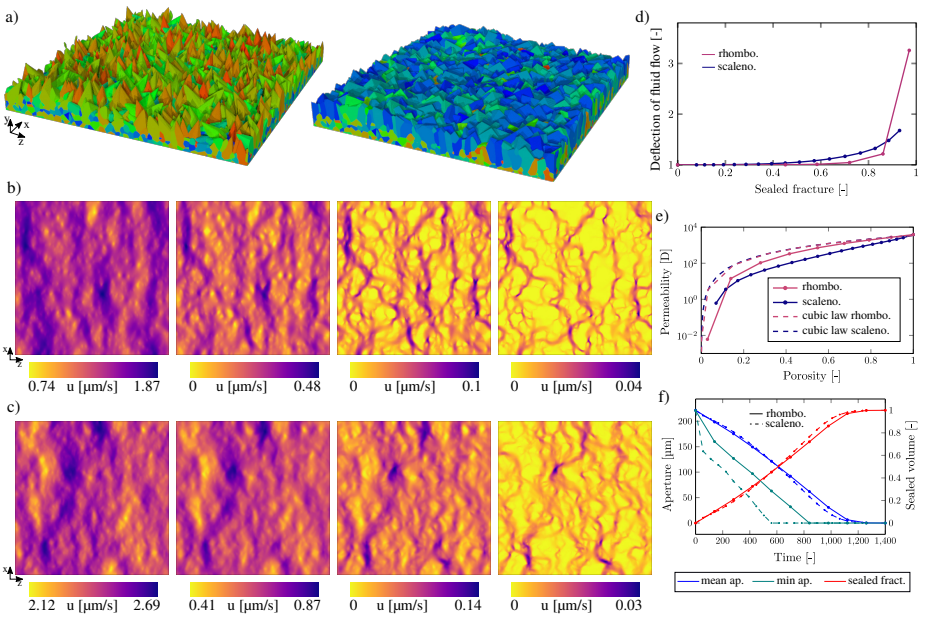

Figure 6: Precipitation of calcite with rhombohedral and scalenohedral crystal shape. a) Lower fracture surface of scalenohedral (left) and rhombohedral (right) calcite during intermediate stage of sealing (same amount of precipitated volume). Fluid flow in b) scalenohedral and c) rhombohedral case for similar amount of precipitated volume. d) Plot of the deflection of the flow path. e) Permeability-porosity relationship for both crystal shapes for measured permeability and calculated permeability with the cubic law (Eq. (10)). f) Minimal and mean aperture during sealing for both crystal habits.

the cubic law is depicted in Fig. 6e. Since the growth front of the rhombohedral case is homogeneous and relatively close to planar plates the deviation from cubic law is low in early stages of sealing and increases once precipitation is advanced and the fracture walls partly touch (Fig. 6f). In the scalenohedral case a deviation from the cubic law is already visible in early sealing stages and deviates stronger in later stages compared to the rhombohedral case. This can be attributed to the inhomogeneous growth front and earlier formation of pillars (and its deviation from planar plates) and the resulting stronger deflection of the fluid (Fig. 6f).

Similarly, as in the previous section we also investigate the difference between the two crystal habits for apertures of 2-10 D_m. The transmissivity evolution of the different apertures with the scalenohedral habit shows a deviation between the simulated transmissivity and the cubic law in early sealing stages and an

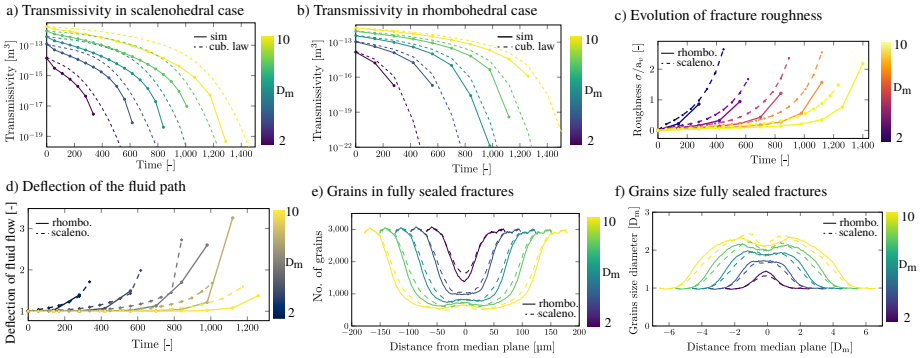

Figure 7: Transmissivity evolution in calcite filled fractures for initial fracture apertures of 2-10 D_m for a) scalenohedral and b) rhombohedral crystal habit. The measured transmissivity from the phase-field simulation (bold line) and the computed transmissivity with the cubic law (dashed line) are plotted. c) Comparison of fracture roughness σ/a_v for both crystal shapes. d) Temporal evolution of the deflection of the flow path τ_h. e) Number of grains and f) crystal size diameter along the fully sealed fractures.

increasing and significant deviation in later times (Fig. 7a). In contrast, the measured transmissivity lies closer to the value predicted by the cubic law for the rhombohedral habit for all apertures. This difference is also visible in the plots of the relative fracture roughness (Fig. 7c). Additionally, the behavior of more interaction of the crystal tips with the fluid flow is illustrated in the trend of the deflection of the flow path in Fig. 7d.
The number of grains in the fully sealed fractures (Fig. 7e) and correspondingly the grain size of the present crystals (Fig. 7f) show a similar trend for both the rhombohedral and scalenohedral habit. However, slightly more scalenohedral grains are present at the same distance from the median line, which can again be attributed to the elongated c-axis of the scalenohedral habit.

3.3. Effect of fracture surface heterogenities

In limestone different fracturing types can occur, namely intergranular, transgranular, and mixed type micro-cracking where grains fracture both inter- and transgranular [60]. In the previous section we analyzed rock structures with pure transgranular fracturing. Here, the effect of heterogeneous fracture surfaces (mixed type micro-cracking) on the transmissivity evolution is investigated. Similar as in the previous works of Spruženiece et al. [60, 61] and Späth et al. [62] we assume a growth rate difference between intergranular and transgranular fractured grains. This may be the result from clay coatings on intergranularly fractured grains, where a fracture cuts through the clay coating and leaves a partial coating on the calcite grains. This partial coating hinders the precipitation rate compared to freshly broken transgranular fractures. The reduced growth rate on intergranular fracture surfaces is modeled with a decrease in the solid/liquid interface mobility. In this section we set the ratio of the mobilities of transgranular to intergranular fractured grains to 20 and use

a fracture surface with 95% intergranular and 5% transgranular fractured host rock grains. This choice gives a good agreement of the simulations with natural micritic veins with wide-blocky crystals [60–62]. We chose these particular values for the percentage of the intergranular fracture surface and the ratio of the mobility since (I) they are in accordance with natural microstructures from Lilstock, UK and (II) they result in an inhomogeneous crystal growth. The aim of this section is the examination of the fluid flow development where an inhomogeneous growth front occurs. For lower values of the fracture surface composition (e.g., 50% transgranular fractured grains) or very small ratios of the mobilities between inter- and transgranular fractured grains similar crystal structures as in Fig. 6,7 would form (and therefore similar fluid flow characteristics).

We compare in the first case rhombohedral crystals with a heterogeneous and

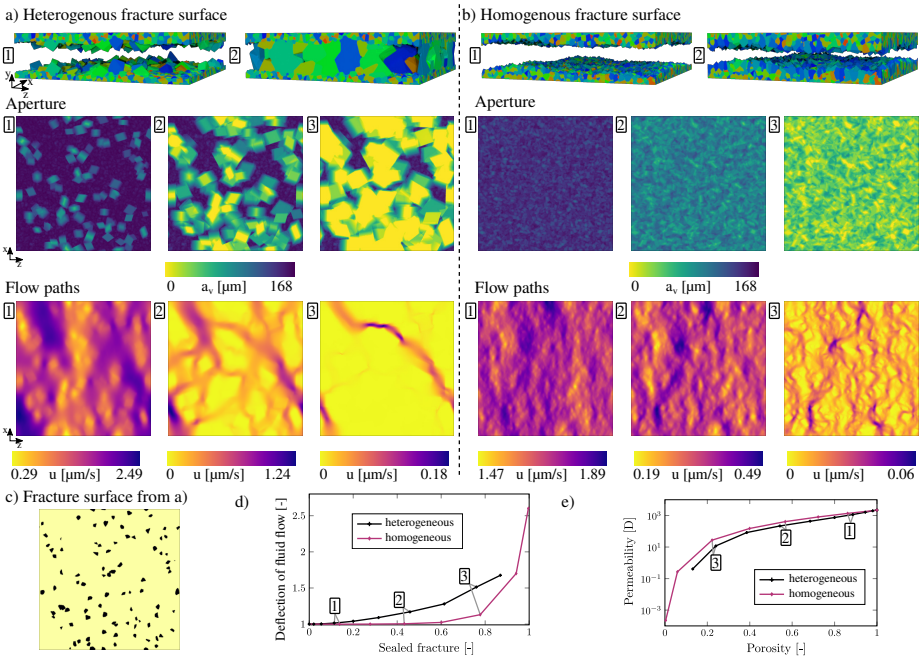

Figure 8: Comparison of fluid flow evolution between a) heterogeneous (inter- and transgranular) and b) homogeneous (pure transgranular) fractured rhombohedral calcite with an initial aperture of $6\,D_m$. The temporal evolution of microstructure (top), remaining aperture in open crack (middle) and flow paths is depicted during stages with a similar volume of precipitated calcite. c) Top view of fracture surface for heterogeneous case in a) with transgranular fractured grains in black and intergranular fractured surface in yellow. d) Evolution of the deflection of the flow path τ_h and e) permeability-porosity relationship for both cases.

homogeneous (pure transgranular) fracture surface for an initial crack aperture of $6\,D_m$. The temporal evolution of the homogeneous and heterogeneous system is depicted in Fig. 8a,b during three time-steps 1 - 3 where a similar amount of calcite precipitated in both cases. The utilized fracture surface for the trans-

granular grains is illustrated in Fig. 8c. In the heterogeneous fracture case the transgranular fractured grains grow faster than the intergranular grains, expand over them and form wide-blocky crystals (c.f. e.g., Spruženiece et al. [60]). This nonuniform and heterogeneous growth front already affects the fluid flow in early sealing stages $\boxed{1}$ and causes blood vessel shaped fluid paths whereas the homogeneous case shows only a slightly deflected stream $\boxed{2}$. In late stages of sealing $\boxed{3}$ the homogeneous case also shows the formation of channels (similar as in Fig. 6c), however still a deviation is visible between the two cases in both the fluid flow and aperture distribution. As a result the deflection of the flow path differs for the two cases in early stages and the difference increases during later sealing states (Fig. 8d). Additionally, the permeability-porosity relationship for the two cases differs (similarly as the scalenohedral shape before) due to the more heterogeneous growth front in the mixed-type (heterogeneous) fracture case (Fig. 8e).

As in the previous sections we perform simulations for initial apertures of 2-10 $\mathrm{D_m}$. In contrast to the homogeneous fracturing case the number of grains in the domain decreases in the heterogeneous case relatively fast due to the growth rate difference and reaches a smaller value since only five percent of the fracture surface contains fast-growing transgranular grains (Fig. 9a). This trend is also in agreement with the 2D simulations in Späth et al. [62]. Furthermore, we observe similar values for the measured transmissivity and the cubic law in the heterogeneous simulations in the early stages (Fig. 9b), however during later sealing states a significant deviation for all fracture apertures is visible due to the inhomogeneous growth front. The corresponding plots for the homogeneous fracturing case are depicted in Fig. 7b,e and show a better resemblance with the cubic law.

Additionally, we measure the number and volume of isolated pores in the open crack for both cases (Fig. 9c,d). For the heterogeneous fracturing case isolated pores form once the transgranular crystal fragments bridge and merge with other fast growing crystals. The number and volume increases until full sealing. Note: There is a decrease of the pore space for the 8 and 10 $\mathrm{D_m}$ case since we utilize a constant driving force in our modeling approach. This results in a continuous sealing (and disappearing of pores) even if a pore is isolated. In contrast, the amount of pores and pore volume is smaller for the homogeneous case, since the growth front is homogeneous and pores mostly occur in later stages when sealing is advanced.

3.4. Determination of the hydraulic apertures during precipitation

The permeability or transmissivity evolution of the fluid flow simulations shows a more or less significant deviation from the cubic law, since it is valid for the permeability estimation of fluid flow between two planar plates. Therefore, when the vertical aperture is used in the computation a deviation can be expected for rough surfaces. When the hydraulic aperture is used in the cubic law, the permeability can be estimated accurately again. Here, we utilize the

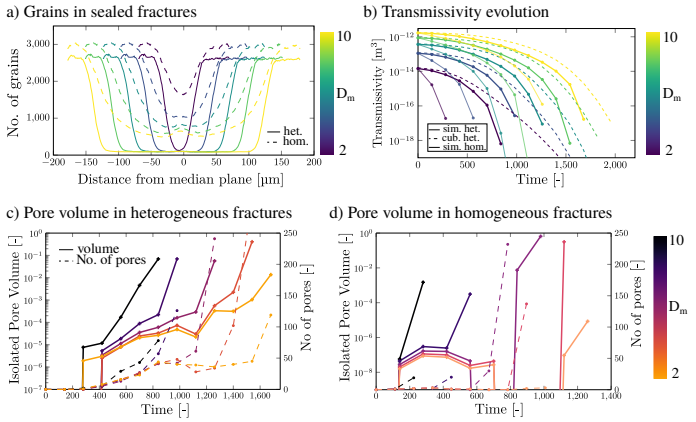

Figure 9: Comparison between homogeneous and heterogeneous fracturing with rhombohedral calcite for initial fracture apertures of 2-10 D_m. a) Number of grains in the simulation domain for the heterogeneous case. b) Transmissivity evolution for the measured values from the simulations and the computed values with cubic law. The corresponding plots for the homogeneous case are depicted in Fig. 7b,e. Number of isolated pores and amount of isolated pore volume for the c) heterogeneous and d) homogeneous fracturing type.

equation for the computation of the hydraulic aperture presented in Kling et al. [34] (Eq. (11)) by calibrating the geometry factor α. Therefore, the effective hydraulic aperture is computed based on the permeability obtained by the fluid flow simulations ($a_{h,sim.} = \sqrt{12k}$, Eq. (10)). The geometry factor α is then calibrated to obtain a good agreement of both hydraulic apertures $a_{h,sim.}$ and $a_{h,Eq.(11)}$. The plots of the vertical and hydraulic apertures a_v, $a_{h,sim.}$ and $a_{h,Eq.(11)}$ are given in Fig. 10. We obtain for the quartz growth study from Sec. 3.1 a geometry factor of $\alpha = 1.45$ (Fig. 10a), for the growth of rhombohedral calcite with a heterogeneous fracture surface form Sec. 3.3 a geometry factor of $\alpha = 0.9$ (Fig. 10b), and for the rhombohedral and scalenohedral calcite growth with a pure transgranular fracture surface from Sec. 3.2 a geometry factor of $\alpha = 1.5$ and $\alpha = 2.5$ respectively (Fig. 10c,d).

The hydraulic apertures in homogeneous rhombohedral calcite case (Fig. 10c) show a sound agreement for all apertures and time-steps and advocate the use of the hydraulic aperture estimation from Eq. (11). However, for other cases (Fig. 10a,b,d) where the evolving crystal shapes and growth fronts are more inhomogeneous we observe an underestimation of the hydraulic aperture with Eq. (11) for the small initial fracture openings and an overestimation of the larger initial fracture openings.

Since theoretical models lead to terms involving $(\sigma/a_v)^2$ in the approximation of the hydraulic aperture [74], we additionally tested the relationships for the hydraulic aperture from Zimmerman et al. [89], Renshaw [90], and a modified version from Kling et al. [34]. However, we observed a larger deviation of the approximated to simulated hydraulic apertures compared to the results shown in Fig. 10 with the original approach of Kling et al. [34] (see Eq. (11)).

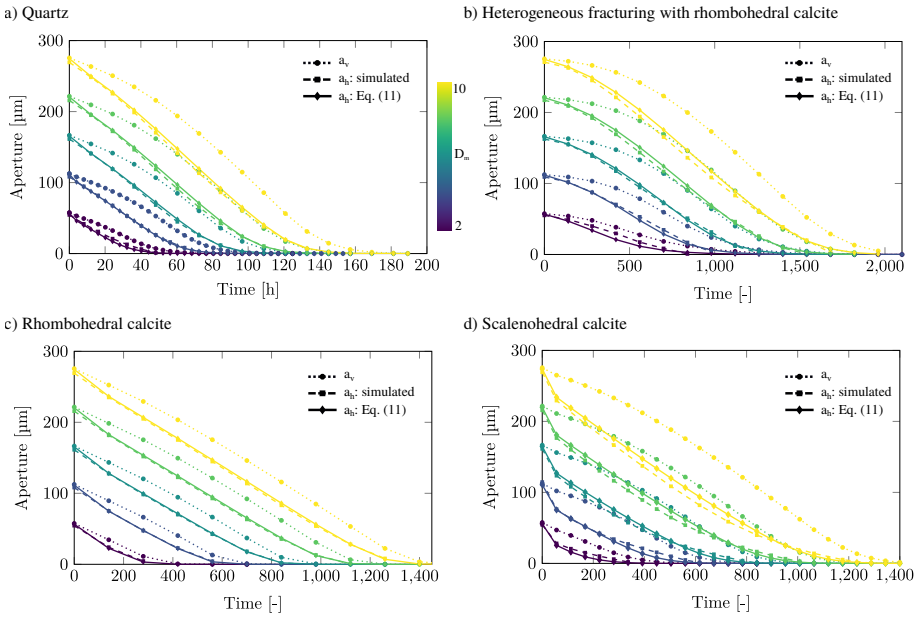

Figure 10: Evolution of vertical and hydraulic apertures for the precipitation of a) quartz (Sec. 3.1), b) rhombohedral calcite with a heterogeneous fracture surface (Sec. 3.3), c) rhombohedral and d) scalenohedral calcite with pure transgranular fracturing (Sec. 3.2). The resulting hydraulic apertures are computed based on the performed fluid flow simulations and with Eq. (11).

3.5. Dissolution of quartz in a partial open fracture

The previous sections discussed the effects of precipitation of different minerals in open fractures on the fluid flow evolution. However, depending on the physical properties of the fluid (e.g., p,c,T) crystal dissolution can also occur in natural subsurface environments. Therefore, we shift the focus of this section to the process of quartz dissolution in a partly open crack. The generation of the host rock and the simulation process is described in Sec. 2.4 and the initial host rock is depicted in Fig. 11a. The numerical host rock is (similarly as in the previous sections) monomineralic, whereas an undersaturated fluid (w.r.t quartz) is assumed to be in contact with the quartz microstructure. We utilize the modeling approach with the corresponding phase-field parameters of Prajapati et al. [67] for faceted quartz dissolution in this section.

The temporal evolution of the polycrystalline quartz microstructure and the fluid flow is given in Fig. 11a during four time-steps ①-④. In the initial stages the fracture walls are partly in contact and result in a deflection of the fluid flow similarly as in the late sealing stage in the previous sections. The quartz crystals in contact with the fluid phase dissolve and cause an increase of the aperture. Fracture walls which are in contact with parts of the opposite fracture wall and have no direct connection to the fluid do not dissolve directly since no remaining fluid channels or pressure solution are considered. Therefore, bridge structures

remain in the open crack and affect the fluid paths (time-step ②). The remaining bridges disappear continuously during the dissolution process. The fracture aperture and fluid flow evolve to a more homogeneous shape over time (time-step ③-④). Nonetheless, remnants of the previously present bridges can still be observed in these later stages and a small influence on the streamlines is still visible.

The mean aperture in the open crack (and therefore also the porosity) increases

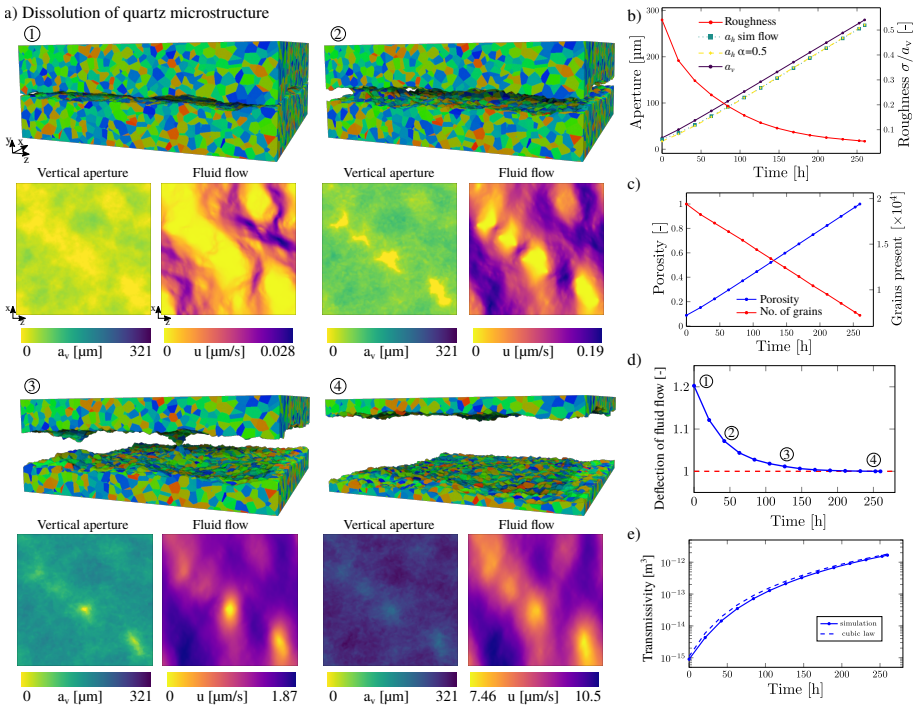

Figure 11: Dissolution of quartz in an open fracture. a) Temporal evolution during four time-steps 1-4. The microstructure (top), the vertical aperture (left) and the fluid flow (right) is given for each step. b) Evolution of vertical a_v and hydraulic apertures a_h and $a_{h,Eq.(11)}$ with α=0.5 and relative surface roughness σ/a_v. Temporal evolution of c) porosity and grains present in the domain, d) deflection of the flow path τ_h, and e) transmissivity.

over time in a nearly linear trend. Similarly, the number of grains present in the system decreases over time (Fig. 11b,c). As expected, the evolution of the relative surface roughness and the deflection of the flow path decrease over time and show an opposite trend as during the crystal growth simulations in the previous sections (Fig. 11b,d). The applied dissolution model results in crystal facets which dissolve with different velocities (Fig. 2d). However, an enhanced dissolution direction or increased dissolution velocity due to the crystal anisotropy is not observed (Fig. 11c) since the crystals are randomly distributed in the host rock and have a similar size. For the transmissivity we observe a relatively small deviation from the cubic law in the beginning and nearly no deviation in

late dissolution stages since close to parallel walls are present during these time steps (Fig. 11e), whereas in intermediate stages where the crystal bridges are present a deviation between the computed cubic law and measured transmissivity is visible.
Here, the hydraulic aperture is also computed with the simulated permeability and the geometry factor α in Eq. (11) is calibrated as in section 3.4. A visibly good agreement of both hydraulic apertures is obtained when $\alpha = 0.5$ is chosen (Fig. 11b).

4. Discussion

The presented work shows the capability of phase-field method in modeling the evolution of microstructures in open fractures during dissolution and precipitation. The evolving crystal structures during precipitation show many similarities to natural microstructures in partly or fully filled fractures (e.g., blocky, stretched, elongated-blocky, wide-blocky grains) which form (e.g. as veins, joints, barren opening-mode fracture) in different subsurface environments, for example in metamorphic rocks and mineral deposits or at low temperature diagenetic settings (e.g., fine scale filling in otherwise open fractures as in [19]). These microstructures are in general agreement with previous studies performed in 2D [17, 42, 59, 60] and 3D [57, 62] and therefore advocate the applicability and validity of phase-field approach in providing accurate insights in crystal evolution processes on microscale.

In this work, we solve the Stokes equations (Eq. (7)) in intermediate crystal growth and dissolution stages and evaluate the permeability evolution. In natural environments both regions with low and high fluid velocities can occur (e.g. in geoscience applications, where fluids are extracted or injected). The Stokes equations loose their validity in regions where turbulent flow occurs, since inertial terms are neglected. Therefore, the results from the permeability calculations cannot directly be applied to regimes with high Re numbers. However, the obtained fluid pathways and evolution of isolated regions should still be applicable in turbulent flow regions. The generated microstructures could be used in later studies by evaluating full Navier-Stokes equations (as in Egert et al. [37]) with the modeling of turbulent flows or by incorporating two/multi-phase flow [91], which then might give further insights into the permeability evolution.

The fluid flow results are used to calibrate the hydraulic aperture from Eq. (11) for the different mineral types during precipitation and dissolution. We observe that this calibrated geometry factor can overestimate the hydraulic aperture for larger and underestimate it for smaller initial apertures (Fig. 10). Therefore, the geometry factor α seems to also have a dependence on other parameters (e.g. initial conditions) and might not be estimated as a constant value. Moreover, in cases of chemically and mechanically active fractures with small aperture increments (e.g., multi-crack-sealing with spanning bridges [17]) the geometry factor might differ again and could also be time-dependent. We computed a different

value for the geometry factor $\alpha = 1.45$ for the *needle quartz* as Kling et al. [34] ($\alpha = 2.5$). This difference could be attributed to the pure intergranular fractured specimen in Kling et al. [34] and the pure transgranular fractures host rock in this work. In the case of pure transgranular fracturing quartz bridges form faster, since two well oriented crystal fragments grow at the opposite fracture walls into the middle and merge (e.g. [17, 18, 62]), whereas in the pure intergranular case one favorably oriented crystal has to bridge nearly the whole open crack to form a crystal pillar. Additionally, the difference might be caused by the domain size difference in this work (e.g., 1000x1000x140µm) and in Kling et al. [34] (150x150x80µm).

In the presented studies a constant over- or undersaturation is assumed in the fluid at all times and we therefore apply a constant driving force for crystal growth or dissolution. However, at some point isolated pores evolve, which do not have a connection to the in-flowing fluid, and further seal until they disappear (which is a limitation of the model). In nature fully sealed fractures are widely observed and therefore, the simulations imply that additional factors control the precipitation at later sealing stages once pores evolve. Different explanations for the (comparatively slower) sealing of pores were discussed in literature, for example diffusion of minerals from the host rock into the open pores [92], remaining fluid flow along nanoscale channels at grain boundaries [93], or full sealing during uplifting (e.g., when partly open fractures are reactivated or new fractures form at weak spots). The modeling could be extended to incorporate some of these factors, by incorporating a reactive flow with a supersaturation dependent driving force.
Moreover, the remaining pores are weaker than the host and could act as nucleation points for new fractures during a renewed loading (e.g., natural or stimulated fluid pulses) or through uplifting. Isolated pores might remain in the rock longer (no connection to fresh fluid) and we speculate that the presence of accessory minerals (Sec. 3.3) or elongated crystal shapes (Sec. 3.2) could be more favorable for re-cracking of partially sealed fractures (due to more isolated pores) and result in multi-crack-sealing. More compact crystal habits (e.g. rhombohedral) with fewer isolated pores, however, might tend to show more delocalized re-fracturing (crack-jump veins [94]).

For the study of quartz dissolution we utilize the phase-field model of Prajapati et al. [67]. This model was set up to depict the process of faceted quartz dissolution. However, since the process of dissolution is highly dependent on the chemical conditions of the fluid and can results in faceted or anhedral bulk dissolution, the present modeling approach could be extended for example by incorporating reactive flow modeling, where the evolving microstructure is directly coupled with the chemical composition of the fluid.
Furthermore, we focus on microstructures with strong grain boundaries in the present work. In natural system the dissolution along grain boundaries might be increased due to weaker bonds, defects, or impurities/accessory minerals. This could also result in detachment of loose grains [95, 96] and influence the

overall permeability evolution. Also, since the quartz microstructure is assumed monomineralic, the effects of faster dissolving accessory minerals and their influence on fluid pathways are not considered, as well as pressure solution in contact areas or fluid channels in regions where fracture surfaces touch.

The presented simulations are performed on microscale where the crystal structure evolution is resolved. The microstructure simulations enable a better understanding of the precipitation and dissolution process at grain scale and how fluid flow interacts in chemically active cracks. In order to obtain insights to length scales which are relevant for geoscience applications (e.g. reservoir scale) an upscaling of the microstructural findings could be approached in later works to explicitly obtain insight on effects of crystal growth on larger length scales. Therein, our modeling approach can be used in combination with upscaling methods (e.g. homogenization techniques or asymptotic expansion as in Ray et al. [47], Bringedal et al. [66], Li et al. [97], Mikelić et al. [98], Choquet and Mikelić [99], Le Borgne et al. [100], Redeker et al. [101]) to improve the understanding of the behavior of fractured or porous rocks on macroscopic length scales over geologic time scales.

5. Concluding Remarks

The present work showcases the versatility and capability of the multiphase-field method in modeling fracture sealing and dissolution processes at microscale. We expand previous phase-field works [34, 60] by utilizing the obtained microstructures to quantify the permeability evolution in chemically active fractures. The systematic phase-field studies on the precipitation and dissolution in single open fractures show the effects of different factors on the fluid flow evaluation as aperture, fracture surface heterogeneities, and crystal habits. Our obtained crystal structures show similarities with microstructures in partly to fully mineral filled opening-mode fractures and can therefore provide insight on how the microstructure evolves and interacts with fluid flow.
Our results reveal that

- the interaction of the fluid and the evolving microstructure depends highly on the crystal habit (Sec. 3.2). An elongated shape results in a more inhomogeneous growth front and therefore stronger deflection of the fluid paths, whereas more compact shapes show less serrated flow paths in early crystallization stages due to the homogeneous growth front.

- during the crystallization different characteristic stages of the fluid flow form. The first stage could be characterized as open region, where fluid flow is not undisturbed, followed by the forest shaped region, where elongated crystals reach in the fluid, and finally a labyrinth shaped region, where sealing is advanced and where the fracture surfaces partly touch and strongly deflect the fluid.

- fluid regions can become isolated from the in-flowing fluid. This depends on parameters as crystal habit and fracture surface. Since natural open fractures can fully seal, additional factors might contribute in these isolated pore regions.
- the dissolution process shows mostly an opposite trend of the precipitation on macroscopic properties (e.g., permeability/transmissivity). Even though a relatively homogeneous surface forms after a while, regions where bridges were present influence the fluid flow until later stages of dissolution.

Acknowledgments

We thank Janos Urai for numerous substantive suggestions in the initial discussions on this research paper. This work was elaborated and completed in his memory. Furthermore, we acknowledge Helmholtz association for funding the research work within the program "MTET: 38.04.04". The authors acknowledge support by the state of Baden-Württemberg through bwHPC. We thank the three anonymous reviewers for theirs constructive reviews.

Research data for this article

The software package PACE3D was used for the generation of the simulation data sets. The software license can be purchased at Steinbeis Network (www.steinbeis.de) in the management of Britta Nestler and Michael Selzer under the subject area "Material Simulation and Process Optimization". The data set, on which this research article is based, can be accessed in the open-access repository at Späth and Nestler [102].

References

[1] S. F. Cox, M. A. Etheridge, V. J. Wall, The role of fluids in syntectonic mass transport, and the localization of metamorphic vein-type ore deposists, Ore Geology Reviews 2 (1987) 65–86.

[2] R. H. Sibson, F. Robert, K. H. Poulsen, High-angle reverse faults, fluid-pressure cycling, and mesothermal gold-quartz deposits, Geology 16 (1988) 551–555.

[3] L. J. Pyrak-Nolte, N. G. W. Cook, D. D. Nolte, Fluid percolation through single fractures, Geophysical Research Letters 15 (1988) 1247–1250.

[4] J. T. Birkholzer, Q. Zhou, C.-F. Tsang, Large-scale impact of CO_2 storage in deep saline aquifers: A sensitivity study on pressure response in stratified systems, International Journal of Greenhouse Gas Control 3 (2009) 181–194.

[5] J. Rutqvist, The geomechanics of CO_2 storage in deep sedimentary formations, Geotechnical and Geological Engineering 30 (2012) 525–551.

[6] C. I. Steefel, S. Molins, D. Trebotich, Pore scale processes associated with subsurface CO_2 injection and sequestration, Reviews in Mineralogy and Geochemistry 77 (2013) 259–303.

[7] J. Rutqvist, Fractured rock stress-permeability relationships from in situ data and effects of temperature and chemical-mechanical couplings, Geofluids 15 (2015) 48–66.

[8] N. Watanabe, N. Hirano, N. Tsuchiya, Diversity of channeling flow in heterogeneous aperture distribution inferred from integrated experimental-numerical analysis on flow through shear fracture in granite, Journal of Geophysical Research: Solid Earth 114 (2009) B04208.

[9] A. Almansour, S. E. Laubach, J. E. Bickel, R. A. Schultz, Value-of-Information Analysis of a Fracture Prediction Method, Society of Petroleum Engineers Reservoir Evaluation & Engineering 23 (2020) 811–823.

[10] B. Berkowitz, Characterizing flow and transport in fractured geological media: A review, Advances in Water Resources 25 (2002) 861–884.

[11] R. Liu, B. Li, Y. Jiang, N. Huang, Mathematical expressions for estimating equivalent permeability of rock fracture networks, Hydrogeology Journal 24 (2016) 1623.

[12] H. S. Viswanathan, J. Ajo-Franklin, J. T. Birkholzer, J. W. Carey, Y. Guglielmi, J. D. Hyman, S. Karra, L. J. Pyrak-Nolte, H. Rajaram, G. Srinivasan, D. M. Tartakovsky, From fluid flow to coupled processes in fractured rock: Recent advances and new frontiers, Reviews of Geophysics 60 (2022) e2021RG000744.

[13] C.-F. Tsang, Coupled hydromechanical-thermochemical processes in rock fractures, Reviews of Geophysics 29 (1991) 537–551.

[14] J. Rutqvist, O. Stephansson, The role of hydromechanical coupling in fractured rock engineering, Hydrogeology Journal 11 (2003) 7–40.

[15] S. E. Laubach, R. H. Lander, L. J. Criscenti, L. M. Anovitz, J. L. Urai, R. M. Pollyea, J. N. Hooker, W. Narr, M. A. Evans, S. N. Kerisit, J. E. Olson, T. Dewers, D. Fisher, R. Bodnar, B. Evans, P. Dove, L. M. Bonnell, M. P. Marder, L. Pyrak-Nolte, The role of chemistry in fracture pattern development and opportunities to advance interpretations of geological materials, Reviews of Geophysics 57 (2019) 1065–1111.

[16] J. G. Ramsay, The crack–seal mechanism of rock deformation, Nature 284 (1980) 135–139.

[17] R. H. Lander, S. E. Laubach, Insights into rates of fracture growth and sealing from a model for quartz cementation in fractured sandstones, GSA Bulletin 127 (2015) 516–538.

[18] M. Späth, J. L. Urai, B. Nestler, Incomplete crack sealing causes localization of fracturing in hydrothermal quartz veins, Geophysical Research Letters 49 (2022) e2022GL098643.

[19] S. R. Forstner, S. E. Laubach, Scale-dependent fracture networks, Journal of Structural Geology 165 (2022) 104748.

[20] J. E. Olson, S. E. Laubach, R. H. Lander, Natural fracture characterization in tight gas sandstones: Integrating mechanics and diagenesis, AAPG Bulletin 93 (2009) 1535–1549.

[21] R. W. Zimmerman, G. S. Bodvarsson, Hydraulic conductivity of rock fractures, Transport in Porous Media 23 (1996) 1–30.

[22] P. A. Witherspoon, J. S. Y. Wang, K. Iwai, J. E. Gale, Validity of Cubic Law for fluid flow in a deformable rock fracture, Water Resources Research 16 (1980) 1016–1024.

[23] R. W. Zimmerman, I.-W. Yeo, Fluid Flow in Rock Fractures: From the Navier-Stokes Equations to the Cubic Law, in: B. Faybishenko, P. A. Witherspoon, S. M. Benson (Eds.), Dynamics of Fluids in Fractured Rock, American Geophysical Union (AGU), 2000, pp. 213–224.

[24] L. A. Thomas, N. Wooster, W. A. Wooster, The hydrothermal synthesis of quartz, Discussions of the Faraday Society 5 (1949) 341–345.

[25] C. B. Cecil, M. T. Heald, Experimental investigation of the effects of grain coatings on quartz growth, Journal of Sedimentary Research 41 (1971) 582–584.

[26] Y.-J. Lee, J. W. Morse, D. V. Wiltschko, An experimentally verified model for calcite precipitation in veins, Chemical Geology 130 (1996) 203–215.

[27] C. Hilgers, K. Dilg-Gruschinski, J. L. Urai, Microstructural evolution of syntaxial veins formed by advective flow, Geology 32 (2004) 261–264.

[28] O. Singurindy, B. Berkowitz, The role of fractures on coupled dissolution and precipitation patterns in carbonate rocks, Advances in water resources 28 (2005) 507–521.

[29] R. H. Lander, R. E. Larese, L. M. Bonnell, Toward more accurate quartz cement models: The importance of euhedral versus noneuhedral growth rates, AAPG Bulletin 92 (2008) 1537–1563.

[30] A. Okamoto, H. Saishu, N. Hirano, N. Tsuchiya, Mineralogical and textural variation of silica minerals in hydrothermal flow-through experiments: Implications for quartz vein formation, Geochimica et Cosmochimica Acta 74 (2010) 3692–3706.

[31] W.-A. Kahl, T. Yuan, T. Bollermann, W. Bach, C. Fischer, Crystal surface reactivity analysis using a combined approach of X-ray micro-computed tomography and vertical scanning interferometry, American Journal of Science 320 (2020) 27–52.

[32] B. Busch, A. Okamoto, K. Garbev, C. Hilgers, Experimental fracture sealing in reservoir sandstones and its relation to rock texture, Journal of Structural Geology 153 (2021) 104447.

[33] Z. G. Philip, J. W. Jennings, J. E. Olson, S. E. Laubach, J. Holder, Modeling coupled fracture-matrix fluid flow in geomechanically simulated fracture networks, Society of Petroleum Engineers Reservoir Evaluation & Engineering 8 (2005) 300–309.

[34] T. Kling, J.-O. Schwarz, F. Wendler, F. Enzmann, P. Blum, Fracture flow due to hydrothermally induced quartz growth, Advances in Water Resources 107 (2017) 93–107.

[35] I. Berre, F. Doster, E. Keilegavlen, Flow in Fractured Porous Media: A Review of Conceptual Models and Discretization Approaches, Transport in Porous Media 130 (2019) 215–236.

[36] S. Marchand, O. Mersch, M. Selzer, F. Nitschke, M. Schoenball, J. Schmittbuhl, B. Nestler, T. Kohl, A Stochastic Study of Flow Anisotropy and Channelling in Open Rough Fractures, Rock Mechanics and Rock Engineering 53 (2020) 233–249.

[37] R. Egert, F. Nitschke, M. Gholami Korzani, T. Kohl, Stochastic 3D Navier-Stokes Flow in Self-Affine Fracture Geometries Controlled by Anisotropy and Channeling, Geophysical Research Letters 48 (2021) e2020GL092138.

[38] A. Paluszny, R. N. Thomas, M. C. Saceanu, R. W. Zimmerman, Hydromechanical interaction effects and channelling in three-dimensional fracture networks undergoing growth and nucleation, Journal of Rock Mechanics and Geotechnical Engineering 12 (2020) 707–719.

[39] J. L. Urai, P. F. Williams, H. L. M. Van Roermund, Kinematics of crystal growth in syntectonic fibrous veins, Journal of Structural Geology 13 (1991) 823–836.

[40] P. D. Bons, Development of crystal morphology during unitaxial growth in a progressively widening vein: I. The numerical model, Journal of Structural Geology 23 (2001) 865–872.

[41] C. Hilgers, D. Koehn, P. D. Bons, J. L. Urai, Development of crystal morphology during unitaxial growth in a progressively widening vein: II. Numerical simulations of the evolution of antitaxial fibrous veins, Journal of Structural Geology 23 (2001) 873–885.

[42] S. Nollet, J. L. Urai, P. D. Bons, C. Hilgers, Numerical simulations of polycrystal growth in veins, Journal of Structural Geology 27 (2005) 217–230.

[43] J. F. W. Gale, R. H. Lander, R. M. Reed, S. E. Laubach, Modeling fracture porosity evolution in dolostone, Journal of Structural Geology 32 (2010) 1201–1211.

[44] A. C. Lasaga, A. Lüttge, Variation of Crystal Dissolution Rate Based on a Dissolution Stepwave Model, Science 291 (2001) 2400–2404.

[45] M. Pollet-Villard, D. Daval, B. Fritz, K. G. Knauss, G. Schäfer, P. Ackerer, Influence of etch pit development on the surface area and dissolution kinetics of the orthoclase (001) surface, Chemical Geology 447 (2016) 79–92.

[46] S. Yang, N. Ukrainczyk, A. Caggiano, E. Koenders, Numerical phase-field model validation for dissolution of minerals, Applied Sciences 11 (2021) 2464.

[47] N. Ray, J. Oberlander, P. Frolkovic, Numerical investigation of a fully coupled micro-macro model for mineral dissolution and precipitation, Computational Geosciences 23 (2019) 1173–1192.

[48] K. Yuan, V. Starchenko, S. S. Lee, V. De Andrade, D. Gursoy, N. C. Sturchio, P. Fenter, Mapping three-dimensional dissolution rates of calcite microcrystals: Effects of surface curvature and dissolved metal ions, ACS Earth and Space Chemistry 3 (2019) 833–843.

[49] Z. Sun, D. N. Espinoza, M. T. Balhoff, Reservoir rock chemo-mechanical alteration quantified by triaxial tests and implications to fracture reactivation, International Journal of Rock Mechanics and Mining Sciences 106 (2018) 250–258.

[50] N. Moelans, B. Blanpain, P. Wollants, An introduction to phase-field modeling of microstructure evolution, Calphad 32 (2008) 268–294.

[51] S. Daubner, M. Weichel, D. Schneider, B. Nestler, Modeling intercalation in cathode materials with phase-field methods: Assumptions and implications using the example of LiFePO4, Electrochimica Acta 421 (2022) 140516.

[52] A. Prahs, M. Reder, D. Schneider, B. Nestler, Thermomechanically coupled theory in the context of the multiphase-field method, International Journal of Mechanical Sciences (2023) 108484.

[53] A. Prahs, L. Schöller, F. K. Schwab, D. Schneider, T. Böhlke, B. Nestler, A multiphase-field approach to small strain crystal plasticity accounting for balance equations on singular surfaces, Computational Mechanics (2023) 1–22.

[54] N. Prajapati, M. Selzer, B. Nestler, Computational modeling of calcite cementation in saline limestone aquifers: A phase-field study, Geothermal Energy 5 (2017) 1–18.

[55] N. Prajapati, M. Selzer, B. Nestler, B. Busch, C. Hilgers, K. Ankit, Three-dimensional phase-field investigation of pore space cementation and permeability in quartz sandstone, Journal of Geophysical Research: Solid Earth 123 (2018) 6378–6396.

[56] N. Prajapati, A. Abad Gonzalez, M. Selzer, B. Nestler, B. Busch, C. Hilgers, Quartz Cementation in Polycrystalline Sandstone: Insights From Phase-Field Simulations, Journal of Geophysical Research: Solid Earth 125 (2020) e2019JB019137.

[57] K. Ankit, J. L. Urai, B. Nestler, Microstructural evolution in bitaxial crack-seal veins: A phase-field study, Journal of Geophysical Research: Solid Earth 120 (2015) 3096–3118.

[58] F. Wendler, A. Okamoto, P. Blum, Phase-field modeling of epitaxial growth of polycrystalline quartz veins in hydrothermal experiments, Geofluids 16 (2016) 211–230.

[59] N. Prajapati, M. Selzer, B. Nestler, B. Busch, C. Hilgers, Modeling fracture cementation processes in calcite limestone: A phase-field study, Geothermal Energy 6 (2018) 1–15.

[60] L. Spruženiece, M. Späth, J. L. Urai, E. Ukar, M. Selzer, B. Nestler, Wide-blocky veins explained by dependency of crystal growth rate on fracture surface type: Insights from phase-field modeling, Geology 49 (2021) 641–646.

[61] L. Spruženiece, M. Späth, J. L. Urai, E. Ukar, M. Selzer, B. Nestler, A. Schwedt, Formation of wide-blocky calcite veins by extreme growth competition, Journal of the Geological Society 178 (2020) 1–17.

[62] M. Späth, L. Spruženiece, J. L. Urai, M. Selzer, M. Arndt, B. Nestler, Kinematics of Crystal Growth in Single-Seal Syntaxial Veins in Limestone-A Phase-Field Study, Journal of Geophysical Research: Solid Earth 126 (2021) e2021JB022106.

[63] M. Späth, J. L. Urai, B. Nestler, Formation of radiator structures in quartz veins - Phase-field modeling of multi-crack sealing, Journal of Structural Geology 158 (2022) 104576.

[64] M. Späth, M. Selzer, B. Busch, D. Schneider, C. Hilgers, J. L. Urai, B. Nestler, Phase-Field Simulations of Epitaxial Crystal Growth in Open Fractures With Reactive Lateral Flow, Water Resources Research 59 (2023) e2023WR034605.

[65] Z. Xu, P. Meakin, Phase-field modeling of solute precipitation and dissolution, The Journal of Chemical Physics 129 (2008) 014705.

[66] C. Bringedal, L. von Wolff, I. S. Pop, Phase field modeling of precipitation and dissolution processes in porous media: Upscaling and numerical experiments, Multiscale Modeling & Simulation 18 (2020) 1076–1112.

[67] N. Prajapati, M. Späth, L. Knecht, M. Selzer, B. Nestler, Quantitative Phase-Field Modeling of Faceted Crystal Dissolution Processes, Crystal Growth & Design 21 (2021) 3266–3279.

[68] A. Kumar, N. Prajapati, M. Späth, B. Busch, D. Schneider, C. Hilgers, B. Nestler, Qualitative Dissolution Modeling of Etch-Pit Formation on the K-Feldspar Surface Through Phase-Field Approach, Journal of Geophysical Research: Solid Earth 128 (2023) e2022JB025749.

[69] B. Nestler, H. Garcke, B. Stinner, Multicomponent alloy solidification: phase-field modeling and simulations, Physical Review E 71 (2005) 041609.

[70] I. Steinbach, Phase-field models in materials science, Modelling and Simulation in Materials Science and Engineering 17 (2009) 073001.

[71] J. Hötzer, A. Reiter, H. Hierl, P. Steinmetz, M. Selzer, B. Nestler, The parallel multi-physics phase-field framework Pace3D, Journal of Computational Science 26 (2018) 1–12.

[72] A. A. Aleksandrov, M. S. Trakhtengerts, Viscosity of water at temperatures of -20 to 150 c, Journal of engineering physics 27 (1974) 1235–1239.

[73] W. M. Haynes, CRC handbook of chemistry and physics, CRC press, 2016.

[74] J. C. Jaeger, N. G. W. Cook, R. Zimmerman, Fundamentals of Rock Mechanics, Blackwell Publishing, 2007.

[75] A. Duda, Z. Koza, M. Matyka, Hydraulic tortuosity in arbitrary porous media flow, Phys. Rev. E 84 (2011) 036319.

[76] V. Goldschmidt, Atlas der Kristallformen, volume 7, C. Winter, Heidelberg, 1922.

[77] L. Schöller, D. Schneider, C. Herrmann, A. Prahs, B. Nestler, Phase-field modeling of crack propagation in heterogeneous materials with multiple crack order parameters, Computer Methods in Applied Mechanics and Engineering 395 (2022) 114965.

[78] A. Bishop, A. Woolley, W. Hamilton, Cambridge guide to minerals, rocks and fossils, Cambridge University Press, Cambridge, 1999.

[79] J. W. Tester, W. G. Worley, B. A. Robinson, C. O. Grigsby, J. L. Feerer, Correlating quartz dissolution kinetics in pure water from 25 to 625°C, Geochimica et Cosmochimica Acta 58 (1994) 2407–2420.

[80] A. J. Gratz, P. Bird, Quartz dissolution: Negative crystal experiments and a rate law, Geochimica et Cosmochimica Acta 57 (1993) 965–976.

[81] P. M. Dove, D. A. Crerar, Kinetics of quartz dissolution in electrolyte solutions using a hydrothermal mixed flow reactor, Geochimica et Cosmochimica Acta 54 (1990) 955–969.

[82] W. G. Worley, J. W. Tester, C. O. Grigsby, Quartz dissolution kinetics from 100–200°C as a function of pH and ionic strength, AIChE Journal (American Institute of Chemical Engineers) 42 (1996) 3442–3457.

[83] F. Jendoubi, A. Mgaidi, M. E. Maaoui, The dissolution kinetics of sand as function of particle size, The Canadian Journal of Chemical Engineering 76 (1998) 233–238.

[84] A. E. Blum, R. A. Yund, A. C. Lasaga, The effect of dislocation density on the dissolution rate of quartz, Geochimica et Cosmochimica Acta 54 (1990) 283–297.

[85] Saupe, Dietmar, Algorithms for random fractals, in: Peitgen, Heinz-Otto and Saupe, Dietmar (Ed.), The Science of Fractal Images, Springer New York, New York, NY, 1988, pp. 71–136.

[86] J. Schmittbuhl, S. Gentier, S. Roux, Field measurements of the roughness of fault surfaces, Geophysical Research Letters 20 (1993) 639–641.

[87] J. Schmittbuhl, F. Schmitt, C. Scholz, Scaling invariance of crack surfaces, Journal of Geophysical Research: Solid Earth 100 (1995) 5953–5973.

[88] S. R. Brown, Fluid flow through rock joints: The effect of surface roughness, Journal of Geophysical Research: Solid Earth 92 (1987) 1337–1347.

[89] R. W. Zimmerman, S. Kumar, G. S. Bodvarsson, Lubrication theory analysis of the permeability of rough-walled fractures, International Journal of Rock Mechanics and Mining Sciences & Geomechanics Abstracts 28 (1991) 325–331.

[90] C. E. Renshaw, On the relationship between mechanical and hydraulic apertures in rough-walled fractures, Journal of Geophysical Research: Solid Earth 100 (1995) 24629–24636.

[91] M. Reder, P. W. Hoffrogge, D. Schneider, B. Nestler, A phase-field based model for coupling two-phase flow with the motion of immersed rigid bodies, International Journal for Numerical Methods in Engineering 123 (2022) 3757–3780.

[92] D. M. Fisher, S. L. Brantley, M. Everett, J. Dzvonik, Cyclic fluid flow through a regionally extensive fracture network within the Kodiak accretionary prism, Journal of Geophysical Research: Solid Earth 100 (1995) 12881–12894.

[93] C. J. Landry, P. Eichhubl, M. Prodanović, S. Wilkins, Nanoscale grain boundary channels in fracture cement enhance flow in mudrocks, Journal of Geophysical Research: Solid Earth 121 (2016) 3366–3376.

[94] R. Caputo, P. L. Hancock, Crack-jump mechanism of microvein formation and its implications for stress cyclicity during extension fracturing, Journal of Geodynamics 27 (1998) 45–60.

[95] S. Emmanuel, Y. Levenson, Limestone weathering rates accelerated by micron-scale grain detachment, Geology 42 (2014) 751–754.

[96] M. Liu, V. Starchenko, L. M. Anovitz, A. G. Stack, Grain detachment and transport clogging during mineral dissolution in carbonate rocks with permeable grain boundaries, Geochimica et Cosmochimica Acta 280 (2020) 202–220.

[97] L. Li, C. A. Peters, M. A. Celia, Upscaling geochemical reaction rates using pore-scale network modeling, Advances in water resources 29 (2006) 1351–1370.

[98] A. Mikelić, V. Devigne, C. J. van Duijn, Rigorous upscaling of the reactive flow through a pore, under dominant peclet and damkohler numbers, SIAM Journal on Mathematical Analysis 38 (2006) 1262–1287.

[99] C. Choquet, A. Mikelić, Rigorous upscaling of the reactive flow with finite kinetics and under dominant péclet number, Continuum Mechanics and Thermodynamics 21 (2009) 125–140.

[100] T. Le Borgne, D. Bolster, M. Dentz, P. de Anna, A. Tartakovsky, Effective pore-scale dispersion upscaling with a correlated continuous time random walk approach, Water Resources Research 47 (2011) W12538.

[101] M. Redeker, C. Rohde, I. Sorin Pop, Upscaling of a tri-phase phase-field model for precipitation in porous media, IMA Journal of Applied Mathematics 81 (2016) 898–939.

[102] M. Späth, B. Nestler, Data set of phase-field studies of permeability evolution in open fractures during precipitation and dissolution [Data set], Zenodo, 2023. URL: `https://doi.org/10.5281/zenodo.8138248`.